TISSUE ENGINEERING: Part A Volume 00, Number 00, 2023 © Mary Ann Liebert, Inc. DOI: 10.1089/ten.tea.2023.0193



Open camera or QR reader and scan code to access this article and other resources online.



Multimodal Three-Dimensional Printing for Micro-Modulation of Scaffold Stiffness Through Machine Learning

Wisarut Kiratitanaporn, PhD,^{1,*} Jiaao Guan, PhD,^{2,*} David B. Berry, PhD,³ Alison Lao, BS,⁴ and Shaochen Chen, PhD^{1,2,4}

The ability to precisely control a scaffold's microstructure and geometry with light-based three-dimensional (3D) printing has been widely demonstrated. However, the modulation of scaffold's mechanical properties through prescribed printing parameters is still underexplored. This study demonstrates a novel 3D-printing workflow to create a complex, elastomeric scaffold with precision-engineered stiffness control by utilizing machine learning. Various printing parameters, including the exposure time, light intensity, printing infill, laser pump current, and printing speed were modulated to print poly (glycerol sebacate) acrylate (PGSA) scaffolds with mechanical properties ranging from 49.3 ± 3.3 kPa to 2.8 ± 0.3 MPa. This enables flexibility in spatial stiffness modulation in addition to high-resolution scaffold fabrication. Then, a neural network-based machine learning model was developed and validated to optimize printing parameters to yield scaffolds with userdefined stiffness modulation for two different vat photopolymerization methods: a digital light processing (DLP)-based 3D printer was utilized to rapidly fabricate stiffness-modulated scaffolds with features on the hundreds of micron scale and a two-photon polymerization (2PP) 3D printer was utilized to print fine structures on the submicron scale. A novel 3D-printing workflow was designed to utilize both DLP-based and 2PP 3D printers to create multiscale scaffolds with precision-tuned stiffness control over both gross and fine geometric features. The described workflow can be used to fabricate scaffolds for a variety of tissue engineering applications, specifically for interfacial tissue engineering for which adjacent tissues possess heterogeneous mechanical properties (e.g., muscle-tendon).

Keywords: 3D printing, two-photon polymerization, digital light processing, machine learning, stiffness

Impact Statement

Fabricating three-dimensional (3D) printed scaffolds with complex stiffness gradients poses a fabrication challenge in light-based 3D printing. In this study, we demonstrate a novel 3D printing workflow that allows for a precise spatial stiffness control over both the macro- and microstructures of 3D printed scaffolds in addition to fine geometrical control over 3D printed scaffold's macroarchitecture. The proposed 3D printing workflow is promising for various applications, including the fabrication of interfacial scaffolds for tissue engineering.

Departments of ¹Bioengineering, ²Electrical and Computer Engineering, ³Orthopedic Surgery, and ⁴NanoEngineering, University of California San Diego, La Jolla, California, USA.

^{*}Both these authors contributed equally to this work.

Introduction

VER THE PAST decade, three-dimensional (3D) printing technology has transformed tissue engineering research and innovation. With many types of additive manufacturing platforms available, fabrication of tissue-engineered scaffolds with complex microarchitectural designs to create biomimetic *in vitro* tissue models and implants has become possible. Per Recently, 3D printing approaches have been applied to fabricate various complex tissues such as vasculature, skin, skin,

Vat photopolymerization technologies, such as digital light processing (DLP)-based 3D printing and two-photon polymerization (2PP)-based 3D printing, are widely used due to their superior printing resolution, speed, and flexible printing pattern input over conventional extrusion- or inkjet-based 3D printing approaches^{8,12} (Fig. 1). Despite their popularity, the use of conventional and light-based 3D printers to fabricate tissue-engineered scaffolds has been mostly confined to the creation of geometrical cues for cell guidance, ^{25,33} various 3D shapes for cell encapsulation, ^{4,11,14} and growth factor incorporation. ³⁴ The 3D printing allows one to deposit cells in specific patterns and

modulate tissues using geometrical cues, mechanical cues, and biological cues. ^{35–43} To create physiologically relevant tissues through 3D printing, scaffolds need to possess necessary geometrical and biological cues with microscale precision to recapitulate the native microenvironment.

In addition, the capability to modulate scaffold stiffness to match that of the native tissue it is attempting to regenerate is equally significant, 40-42 as microscale durotactic cues govern cellular migration and differentiation through contact-mediated guidance from focal adhesion between cells and the microenvironment through rigidity mechanosensing. 37-43

Scaffold stiffness modulation is commonly achieved through the modulation of crosslinker concentration, 44 degree of acrylation, 45,46 and material selection. 47-51 However, these methods can be quite time-consuming, difficult to control, and economically inefficient. In addition, the creation of scaffolds with complex stiffness gradients or regions can pose a fabrication challenge. In light-based 3D printing, various printing parameters such as the printing speed, light intensity, and exposure time can be easily adjusted. However, the relationship between those printing parameters and the resulting mechanical properties is yet to be studied across different printers and various printing materials.

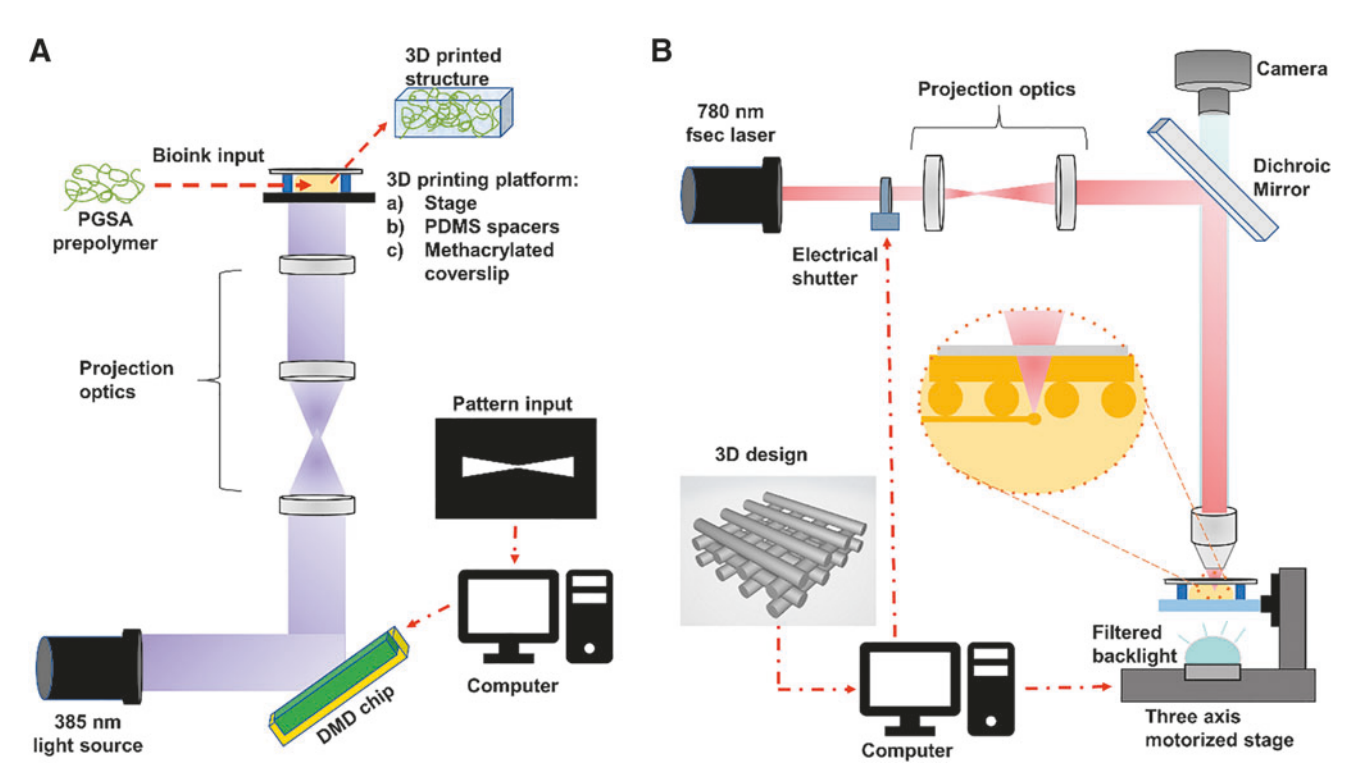


FIG. 1. Schematics for light-based 3D printers. (**A**) Schematic for DLP-based 3D printer. Digital masks with arbitrary geometrical design were continuously uploaded through the synchronized computer-machine system, and the micromirrors inside the DMD chip would flip on or off according to pattern uploaded. A 385-nm light source projected light onto the DMD chip and was reflected off into a group of projection optics, which directed and guided the patterned light into the 3D printing platform containing the PGSA prepolymer reservoir between the PDMS spacers and below the methacrylated coverslip. The patterned light crosslinked PGSA prepolymer into a scaffold with patterned structure. (**B**) Schematic for 2PP 3D printer. The 780 nm femtosecond laser projected a high-power laser through the projection optics and the objective lens onto the top of the photo-ink, where the photo-ink was polymerized on the methacrylated coverslip. The polymerized patterns were guided by the three-axis motorized stage and the electrical shutter controlled by a computer program. 2PP, two-photon polymerization; 3D, three-dimensional; DLP, digital light processing; DMD, digital micromirror device; PDMS, polydimethylsiloxane; PGSA, poly (glycerol sebacate) acrylate.

In this study, poly (glycerol sebacate) acrylate (PGSA) was selected to demonstrate how 3D printing parameters can be modulated to precisely tailor the stiffness of a scaffold over several orders of magnitude. PGSA is compatible with both DLP and 2PP light-based 3D printing systems 13,33,44,46,52 and its tough, robust mechanical properties make it an attractive materia musculoskeletal tissue engineering applications. 13,33,44–46,52–61

With recent advances on machine learning, this efficient data analysis approach has been actively studied in many experimental engineering fields, including 3D printing. Previously we have introduced a machine learning assisted tool to enhance the printing fidelity of DLP-based 3D printers affected by the light scattering effect in both acellular and cellular scaffolds. Among the previous studies, the major focus of machine learning in 3D printing was on analyzing the structural and morphological aspect, while the manipulation of mechanical properties of printed were underexplored. In our study, we apply a neural network (NN)-based machine learning model to study the mechanical properties of scaffolds fabricated under a range of printing parameters and 3D printers. A fully trained NN model would provide a novel method to precisely modulate digital stiffness for precision tissue-engineered scaffold fabrication.

Utilizing the advantages of multiple 3D printing systems, a new workflow to fabricate precision-engineered scaffolds is introduced (Fig. 2). This approach combines macroscopic DLP-based 3D printing to create scaffolds with geometric features on the hundreds of micron scale, followed by the decoration of the scaffold with submicron features fabricated using a 2PP-based 3D printing system. Together with the machine learning algorithm, this workflow (Fig. 2) enables simultaneous control over both geometric cues and mechanical cues during the light-based 3D printing process to engineer scaffolds with tunable geometric features ranging from 1 µm to 1 mm and material properties ranging from kPa to MPa.

Methods

Materials

Ethyl acetate, glycerol, and sebacic acid were purchased through Fisher Scientific (Waltham, MA). Acryloyl chloride, triethylamine (TEA), 4-dimethylaminopyridine (DMAP), anhydrous dichloromethane (DCM), diphenyl(2,4,6-trimethylbenzoyl)phosphine oxide (TPO), fluorescein sodium salt, and tartrazine were purchased through Millipore Sigma (St. Louis, MO).

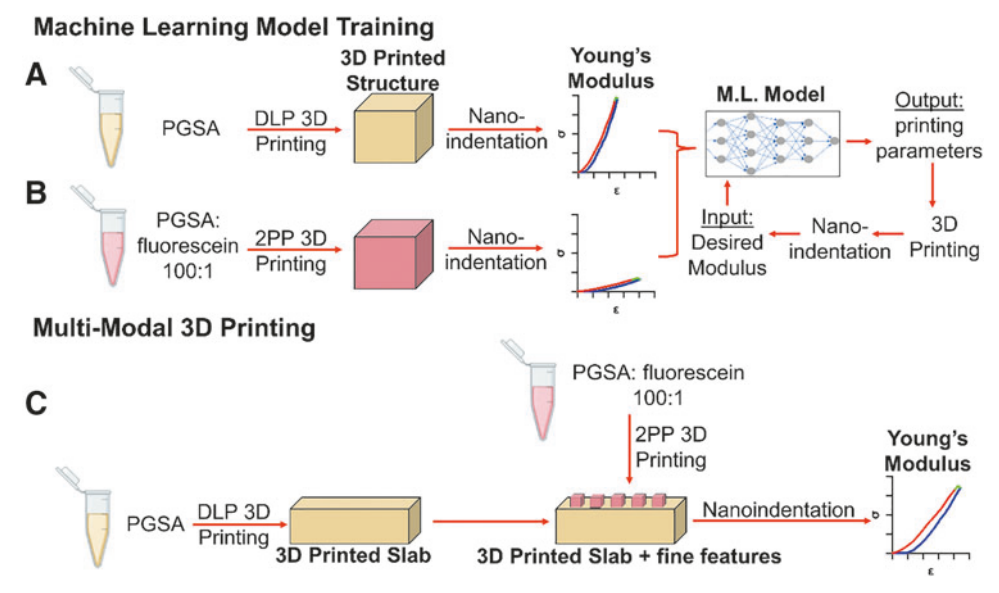


FIG. 2. Schematics outlining the research strategies employed. (A) PGSA prepolymer underwent polymerization at various printing parameters through DLP-based 3D printing. (B) PGSA prepolymer underwent polymerization at various printing parameters through 2PP 3D printing. Structures 3D printed at varying parameters then underwent nanoindentation to investigate the effect of printing parameters on the Young's modulus of the printed structure. The Young's modulus data was then fed into a machine learning model, which then output printing parameters for either a DLP-based 3D printer or 2PP-based 3D printer that would fabricate structures possessing intended stiffness values (values which served as input into the machine learning model). Once the 3D structures were printed according to the NN model-generated printing parameters, they underwent nanoindentation testing to compare the measured Young's modulus versus the target Young's modulus values (input values into the machine learning model). (C) PGSA prepolymer underwent sequential, multiprinter 3D printing process to fabricate complex scaffolds possessing hundreds of micron structures (printed through DLP-based 3D printing) with submicron features (printed through 2PP-based 3D printing) and investigate and verify that independent stiffness control was possible for each modular printed structure. PGSA base matrices, which were either soft or stiff, were printed through DLP-based 3D printing. Microstructures printed through 2PP-based printing were then printed on top of the base matrices and subjected to nanoindentation testing to verify that the microstructure stiffness printed through the 2PP platform was independent of the substrate or base matrix stiffness printed through the DLP-based printing platform. This serves to verify that the control of 2PP microstructure stiffness is possible in a multiprinter hybrid print.

PGS synthesis

PGS synthesis was based on a previously published protocol.¹³ Under constant argon gas flushing, sebacic acid and glycerol were mixed in a 1:1 equimolar ratio at 140°C with constant stirring for 1h until they are evenly melted and mixed. After that, the temperature was reduced to 120°C, and pressure was set to 35 Pa for the polycondensation reaction to occur. The pressure of 35 Pa was maintained throughout the 15-h period for the polycondensation reaction.

PGSA synthesis

To create PGSA, PGS underwent an acrylation reaction according to a previously published protocol. 13 Under argon atmosphere and constant stirring, 300 mL of DCM was added to 30 g of PGS to fully dissolve it. After 1 h, 30 mg of DMAP was added to the mixture under argon gas. Once the temperature was reduced to 0°C, dropwise addition of 7 mL of TEA was performed, which was followed by the addition of 3.3 mL of acryloyl chloride in a dropwise manner. Under the dark, acrylation reaction was carried out for the next 24 h at room temperature. Rotary evaporation at 40°C was then used to remove DCM from the solution. This was followed by the precipitation of TEA through the addition of excess ethyl acetate. Finally, the prepolymer solution was filtered and rotary evaporated at 45°C and 5 Pa to remove the remaining excess ethyl acetate. PGSA was then stored at -20°C until use. PGSA compound used in this study was from the same batch used in a previously published literature with 57% of acrylation. 13

PGSA-based printing solution preparation

To make the PGSA prepolymer solution printable with DLP-based 3D printing platform, the PGSA prepolymer solution was mixed with 4% (w/v%) TPO and 0.01% (w/v%) tartrazine. The resulting PGSA solution was further mixed with sodium fluorescein at 100:1 dilution to provide fluorescent tracing for the 2PP 3D printer.

3D printing of PGSA through DLP-based 3D printing system

The first 3D printer we used was an in-laboratory-developed DLP-based 3D printing system. ¹² The system contains multiple main components, including 385 nm light source (Hamamatsu Photonics), digital micromirror device (DMD) chip (Texas Instruments, Dallas, TX) for light pattern control, projection optics for light guidance, a static printing stage serving as the prepolymer reservoir, and specialized computer software for controlling projected photomasks, light intensity, exposure time, and hardware synchronization. The digital patterns were created through an in-house-developed MATLAB script and were then uploaded as BMP files to the specialized 3D printing software.

Setup of the DLP-based 3D printing platform consisted of two 300-µm-thick polydimethylsiloxane (PDMS) spacers with methacrylated glass coverslip located on top and PDMS-coated static stage located at the bottom of the PDMS spacers. The PGSA prepolymer solution was then injected in between the PDMS spacers through a positive pressure pipette. Then, the 385 nm light was projected from the light source to the DMD chip to form a pattern, and

through optical projection lens into the PGSA prepolymer solution at specific exposure time and light energy density. The printed scaffold was then washed and rinsed in isopropyl alcohol (IPA), deionized water, and phosphate-buffered saline (PBS).

2PP 3D printing

The in-lab 2PP 3D printing system was composed of a 780 nm femtosecond laser (Calmar Laser), projection optics, a three-axis digital control system made of motorized linear stages and a motion controller (Newport Corp.), a digital shutter (Sutter Instrument), a $50 \times / \text{NA}$ 0.5 objective lens (Carl Zeiss AG), and a desktop computer with custom software control system written in C# to control the shutter and stages (Fig. 1). After the software read a G-Code script to guide the stage movement path and shutter controls, the open-source slicing software Slic3r (Slic3r v.1.3.0) was used to generate G-Code from 3D models.

The printing platform consisted of a microscope glass slide, two 250 µm PDMS spacers, and a methacrylated glass coverslip on top. The photo-ink was injected in between the PDMS spacers. The printing platform was then placed on top of the digital stage system for controlled movement. The femtosecond laser projected a high-power laser through the projection optics and the objective lens onto the top of the photo-ink, which is in contact with the coverslip, and the photo-ink polymerized on the methacrylated coverslip. Note that due to the femtosecond laser pulses, polymerization only happens in a tiny region at the focal point of the laser beam where just enough energy was deposited to execute the photopolymerization process, enabling ultrahigh-resolution printing of submicron structures. After that, the stage moves based on the given path defined by G-Code, and the photoink gradually polymerizes to create the complete 3D structure from the coverslip downward into the photo-ink while the shutter controls the laser on and off. After printing, the printed scaffolds were washed and rinsed in IPA (Fig. 3).

Combining DLP-based 3D printing with 2PP 3D printing

After the capabilities of the DLP-based 3D printer and the 2PP printer were investigated, a combined printing process, which utilized the rapid fabrication speed of the DLP printer to make complex scaffolds hundreds of microns in scale and the 2PP printer to decorate structures of submicron to a few microns in size on top of the DLP printed scaffolds, was demonstrated.

Once the PGSA base matrix was printed through DLP-based 3D printing platform (3D printing of PGSA through DLP-based 3D printing system), the 3D printed scaffold was washed with IPA and air dried. Then, a printing platform for the 2PP printer was prepared in the same manner as previously described in 2PP 3D printing, except that the methacrylated coverslip was replaced by the one with DLP printed scaffold on it. The coverslip was placed with DLP-printed scaffolds facing downward. The DLP-printed scaffolds were then carefully immersed into the fluorescein-PGSA prepolymer ink (1:100 dilution). After that, the 2PP laser polymerized the photo-ink on the surface of the DLP scaffold, resulting in the fabrication of a complex large scaffold with submicron fine features.

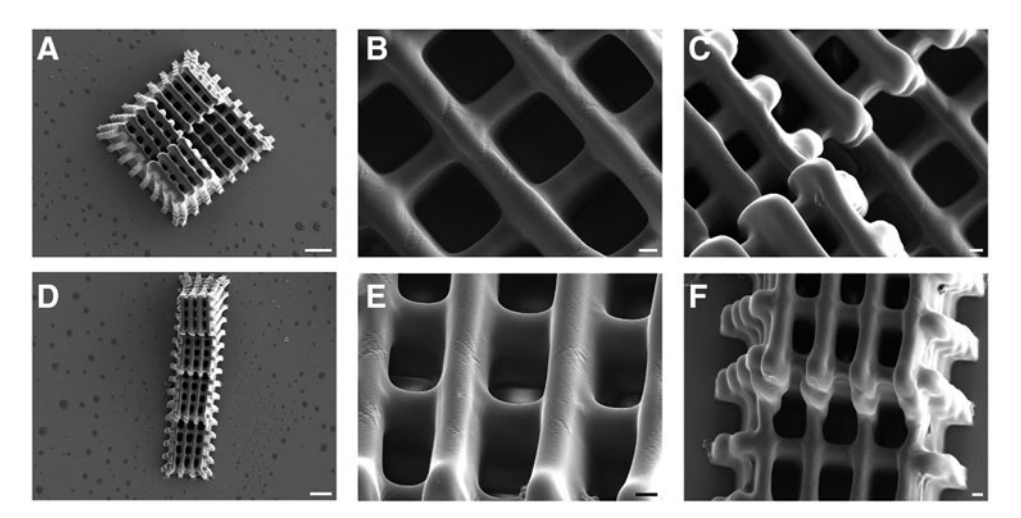


FIG. 3. SEM images of 3D-printed PGSA structures through 2PP. (**A**) SEM image of printed log-pile spiral staircase of different heights. (**B**) SEM image of the zoomed-in view of the log-pile unit demonstrated in (**A**). (**C**) SEM image of the zoomed-in view of the middle of the log-pile spiral staircase demonstrated in (**A**). (**D**) SEM image of the straight log-pile staircase of different heights. (**E**) SEM image of the zoomed-in view of the individual log-pile unit imaged at 20° angle. (**F**) SEM image of the zoomed-in view of the junction between two log-pile stairs in (**D**) to demonstrate the height difference. Scale bars are 20 μm for (**A**, **D**), and 2 μm for (**B**, **C**, **E**, **F**). SEM, scanning electron microscopy.

Nanoindentation

The Young's moduli of the 3D printed PGSA-based specimens were measured using a Piuma nanoindenter (Optics11 Life). To prepare the samples for nanoindentation, all the samples were glued to the bottom of the Petri dish and submerged in PBS solution before testing. The nanoindentation test was carried out at room temperature. For all the nanoindentation experiments, a spherical probe with cantilever stiffness k = 4.24 N/m and tip radius r = 48.5 μ m was used. Hertz contact model⁶⁵ and a Poisson's ratio of $0.5^{33,66}$ were assumed for this study for data analysis purposes. For each sample, at least three indentations were carried out and the results were averaged. For each experimental condition, 5-10 individual samples (n = 5-10) were tested.

PGSA rectangular nanoindentation specimens measuring $2\,\text{mm} \times 2\,\text{mm} \times 300\,\mu\text{m}$ fabricated through DLP-based printing system, and specimens measuring $400 \times 400 \times 10\,\mu\text{m}$ were fabricated through 2PP printing. The printing parameters used can be found in Tables 2 and 3. All printed specimens were subjected to nanoindentation for Young's modulus measurement to analyze the effect of 2PP printing parameters on printed scaffold stiffness (Fig. 4).

Machine learning

For each 3D printing system, once we obtained the Young's modulus values of the 3D printed samples, a fully connected NN model was applied to learn the correlation between the printing parameters and the scaffold stiffness. The resulting trained model was able to predict the sample stiffness with any given set of printing parameters. ⁶⁷ On top of that, any desired sample stiffness could be achieved by brute-force searching from the possible printing parameter combinations according to the trained NN predictions.

The fully connected NN model, also named as multilayer perceptron, was composed of an input layer with the printing parameters, three hidden layers with 20, 10, and 5

neurons, and an output layer with a single neuron representing the predicted Young's modulus as a scalar value (Fig. 2). Each neuron calculates the weighted linear summation of the previous layer neurons plus a bias variable. A rectifying linear unit (ReLU) activation function was also applied to hidden layer neurons to allow the NN model to predict nonlinear relationship.⁶⁸

The NN model was programmed in Python with the Py-Torch package. ⁶⁹ The NN model training applied the Adam optimizer to optimize the model weights and biases based on mean square error between the model output and the measured stiffnesses. ⁷⁰ After training, the NN model could accurately predict the scaffold stiffness for arbitrary printing parameters. A brute-force searching method was then applied to search for any desired scaffold stiffness values and their corresponding printing parameters (Fig. 5).

Statistical analyses

All statistical analyses were performed using GraphPad Prism 9 (GraphPad Software). To determine the effect of 3D printing parameters, including the light intensity, exposure time, printing infill, printing current, printing speed on Young's modulus, and one-way analysis of variance (ANOVA) with *post hoc* Sidak's tests with multiple comparisons were performed to compare the tested groups. To compare the accuracy of the NN model to the actual mechanical properties' measurement, the coefficient of variation (R^2) of the measured stiffness was calculated with respect to the predicted data from the NN model. Differences between treatment groups were considered significant when p < 0.05. All data are reported as mean \pm standard deviation.

Experiment

3D printing of PGSA

The capability of DLP 3D printers to fabricate PGSA 3D scaffolds with dimensions tens of microns up to centimeters

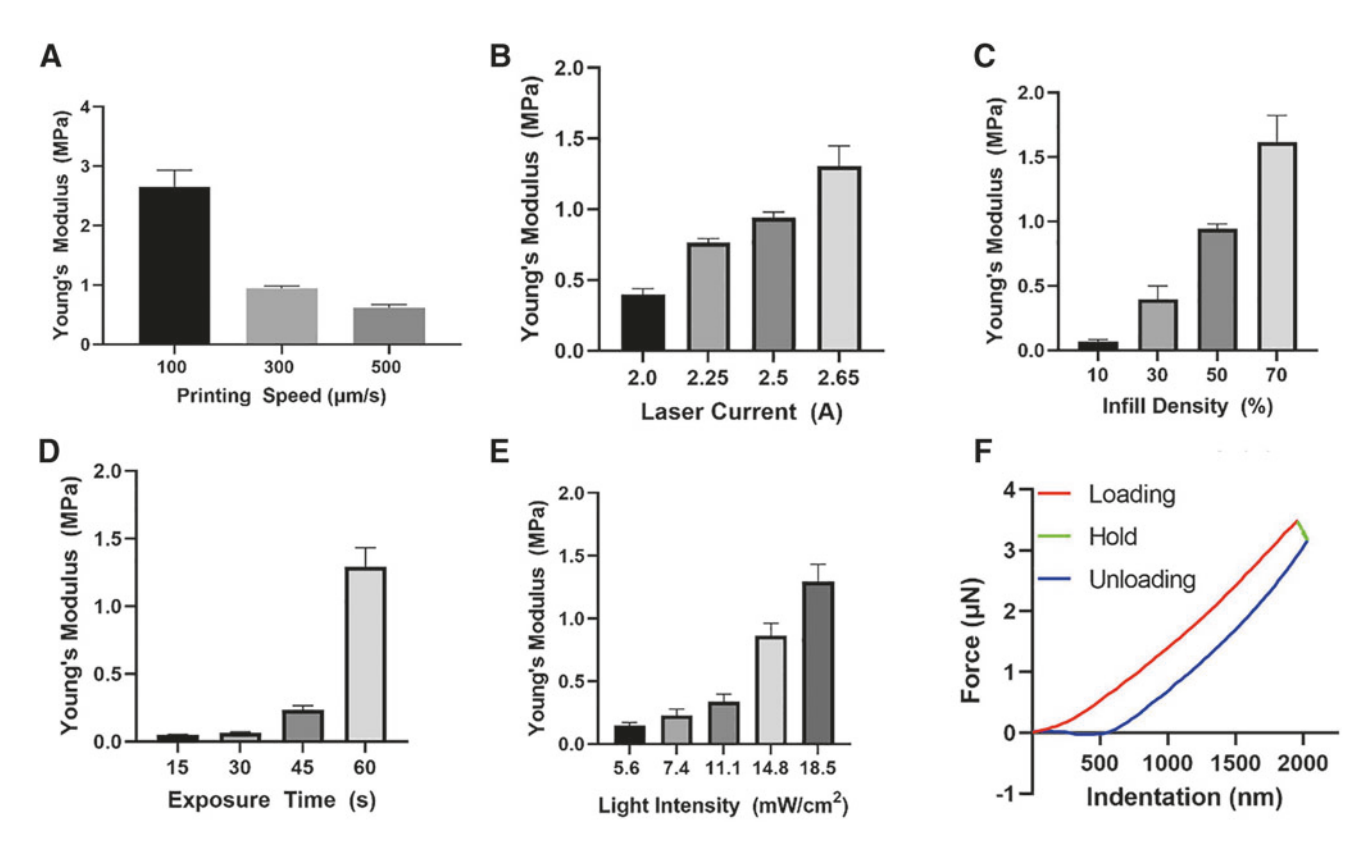


FIG. 4. Young's Modulus for 2PP (**A–C**) and DLP (**D, E**) printed structures, and a sample stress and strain curve (**F**). (**A**) Young's modulus of structures 3D printed through 2PP as a function of printing speed. Significant effect of printing speed on scaffold stiffness was observed. (p < 0.0001). Sidak's *post hoc* test revealed significant differences between each printing speed (p < 0.0119). (**B**) Young's modulus of structures 3D printed through 2PP as a function of laser current. Significant effect of laser current on scaffold stiffness was observed (p < 0.0001). Sidak's tests revealed significant differences between each laser current (p < 0.0025). (**C**) Young's modulus of structures 3D printed through 2PP as a function of infill density. Significant effect of infill density was observed (p < 0.0001). Sidak's tests revealed significant differences between each infill density (p < 0.0005). (**D**) Young's modulus of structures 3D printed through DLP-based 3D printing as a function of exposure time. Significant effect of exposure time on scaffold's Young modulus was observed (p < 0.0001). (**E**) Young's modulus of structures 3D printed through DLP-based 3D printing as a function of exposure time. Significant effect of light intensity on scaffold stiffness was observed (p < 0.0001). (**F**) Stress–strain curve of a structure 3D printed through 2PP at 300 μm/s printing speed.

has been previously reported. 13,44 The 2PP 3D printer demonstrated the ability to print PGSA 50 μ m log-pile structures. Individual logs had a 2 μ m width while keeping a 5 μ m hollow cavity region around the logs (Fig. 3). Additionally, micro-ring structures with a 2 μ m inner diameter and 1 μ m lateral line thickness were fabricated (Supplementary Fig. S1).

Using the in-house-developed DLP and 2PP 3D printing systems, the ability to efficiently 3D print complex scaffolds hundreds of microns in size using a DLP printer with finer features at submicron scale printed on top by a 2PP printer was demonstrated. Following the workflow in Combining DLP-based 3D printing with 2PP 3D printing, the combined printing process with both printers could be achieved, whereby a 2PP printer was used to fabricate fine detailed decorations on top of the bulk DLP printed scaffolds. A simple cubic 2PP structure was printed on top of another larger cubic DLP printed scaffold, which was later mechanically tested. Additionally, a complex muscle—tendon microstructure design was fabricated based on a transmission electron microscopy (TEM) image of a myotendinous junction (MTJ) tissue section (Fig. 6).

Digital modulation of mechanical properties through the adjustment of DLP-based 3D printing parameters: exposure time and light intensity

An investigation to explore the range of mechanical properties of PGSA that could be achieved through the tunable printing parameters of DLP-based 3D printing was performed.

First, the effect of exposure time used during DLP-based 3D printing on resulting PGSA scaffold stiffness was explored, as exposure time had been shown to be directly associated with crosslinking density 71,72 and was a printing parameter that can be easily adjusted. PGSA scaffolds were printed with 15, 30, 45, and 60 s exposure times while the light intensity was kept constant during the printing process at $18.5 \, \mathrm{mW/cm^2}$. The resultant Young's modulus values are shown on Table 1 and Figure 4D. A significant effect of exposure time on scaffold stiffness was observed (p < 0.0001). Post hoc tests revealed significant differences between all exposure times (p < 0.0002), except for $15 \, \mathrm{s}$ versus $30 \, \mathrm{s}$ exposure. These results indicate that the Young's modulus of PGSA can be precisely tuned through varying exposure time during DLP printing.

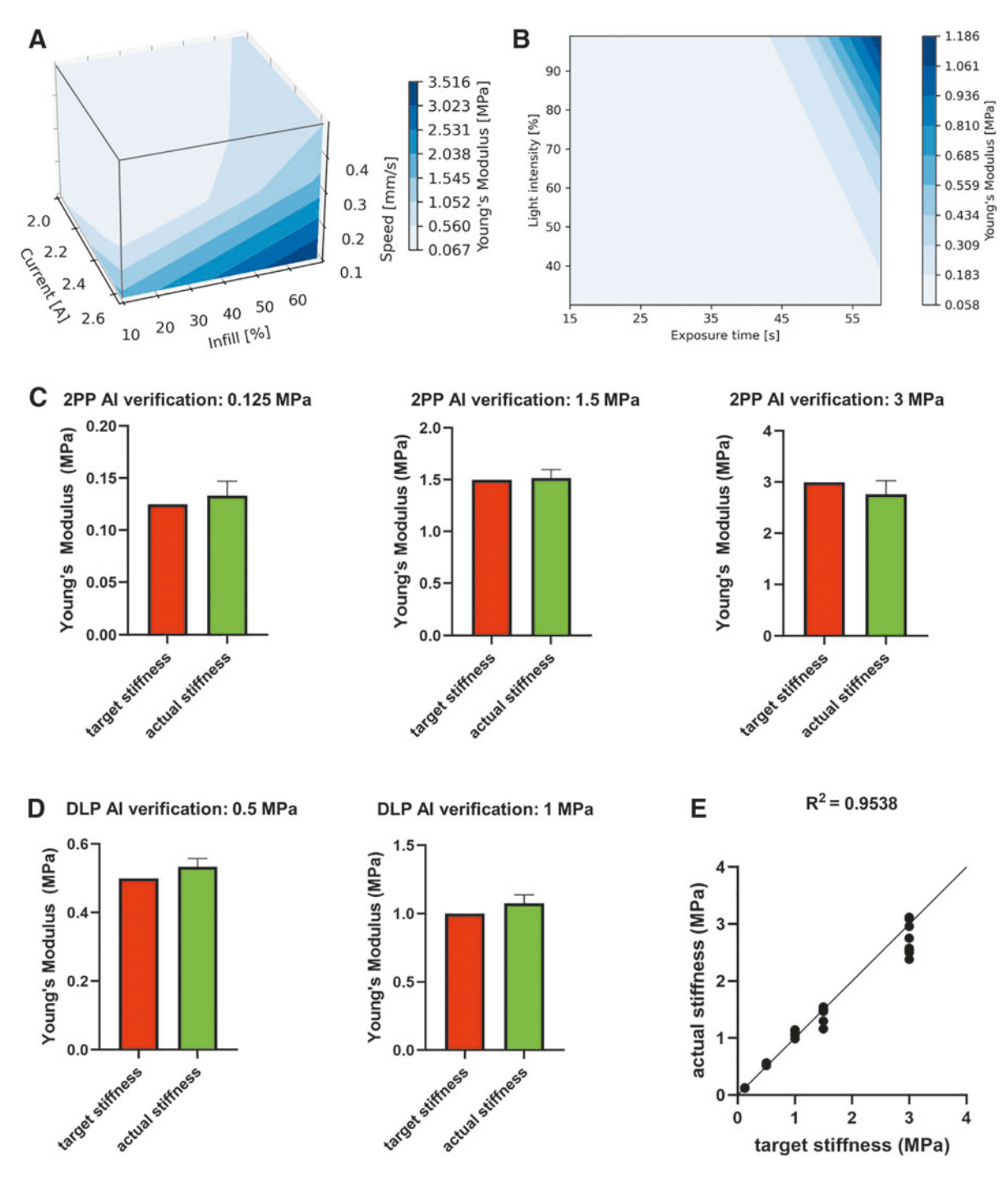


FIG. 5. Machine learning result and verification. (**A**) The 3D heat map representing the stiffness distribution with respect to the changes of three 2PP printer parameters, namely printing speed, laser current, and infill density. (**B**) The 2D heat map representing the stiffness distribution with respect to the changes of two DLP printing parameters, namely exposure time and light intensity. (**C**) The comparison between the desired stiffness and the 2PP printed sample stiffness using printing parameters generated by machine learning for 0.125, 1.5, and 3 MPa, respectively. (**D**) The comparison between the desired stiffness and the DLP printed sample stiffness using printing parameters generated by machine learning for 0.5 and 1 MPa, respectively. (**E**) The uniformity plot where the points represent the actual measured stiffness of the printed samples versus the target stiffness, and the coefficient of determination for all the data points on the plot. 2D, two-dimensional.

In addition, the influence of light intensity adjustment on scaffold stiffness was investigated. PGSA mechanical testing specimens were printed with light intensities of 5.6, 7.4, 11.1, 14.8, and 18.5 mW/cm² at 60 s exposure time. The Young's modulus of tested PGSA scaffolds can be found on

Table 1 and Figure 4E. From Figure 4E, a correlation between light energy density used during the DLP-based 3D printing process and Young's modulus of the printed scaffold was observed. As light energy density used for DLP printing of PGSA increased, the stiffness of the printed

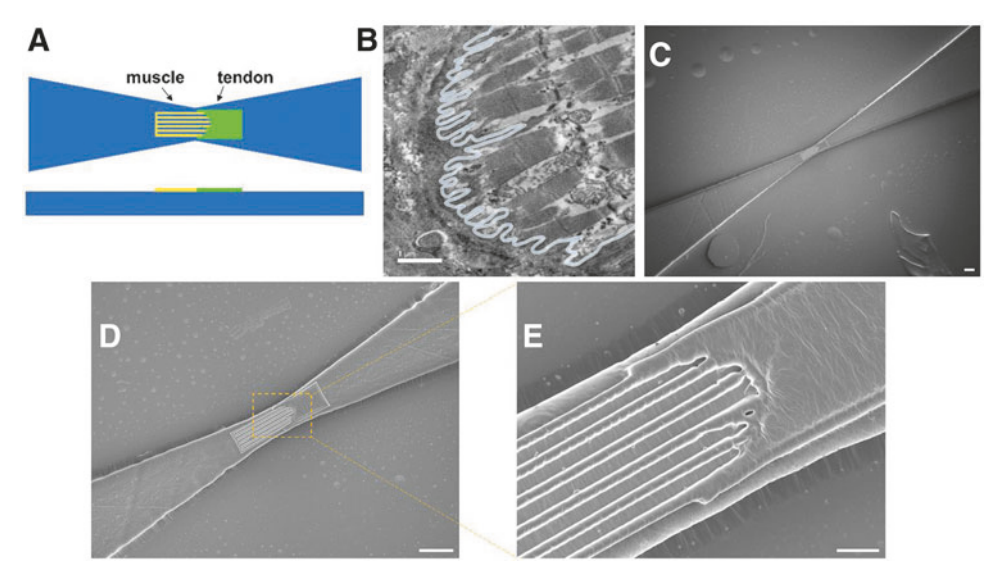


FIG. 6. Design and combined fabrication of DLP and 2PP 3D printing for engineering design of MTJ. (**A**) The engineering design of a two-segment structure to showcase the combined DLP and 2PP printing process. The ribbon-shaped structure was designed for DLP printer, and the muscle and tendon structures were designed for 2PP printer. (**B**) The TEM image of a MTJ region with the outline separating the muscle and tendon regions. (**C**) The SEM image of a 3D printed engineering design (**A**). (**D**) A zoomed-in view of (**C**). (**E**) A zoomed-in view of (**D**). The scale bar is 1 μm for (**B**), 100 μm for (**C**, **D**), and 20 μm for (**E**). MTJ, myotendinous junction; TEM, transmission electron microscopy.

scaffold also increased and *vice versa*. Interestingly, a large increase in the Young's modulus of printed PGSA was noted for the light intensity between 11.1 to 14.8 mW/cm², suggesting a nonlinear relationship between the light intensity and resulting scaffold stiffness.

An ordinary one-way ANOVA statistical analysis revealed a significant effect of the light intensity used during DLP-based 3D printing on PGSA scaffold's stiffness (p < 0.0001). Significant differences between different light intensities on scaffold stiffness were found for most groups (p < 0.0067), with the exception of 5.6 mW/cm² versus 7.4 mW/cm² (p = 0.5924) and 7.4 mW/cm² versus 11.1 mW/cm² (p = 0.2436). These results suggest that mechanical properties of PGSA scaffolds fabricated through DLP-based 3D printing can be precisely manipulated by adjusting the light

Table 1. Experimental Stiffness Measurements of Digital Light Processing-Based Printed Structure and the Corresponding Printing Parameters

	Printing	g parameters		
3D printing system	Exposure time (s)	Light intensity (mW/cm ²)	Measured stiffness	
DLP-based	15	18.5	49.3 ± 3.3 kPa	
	30	18.5	$67.1 \pm 5.9 \text{kPa}$	
	45	18.5	$236.0 \pm 30.6 \mathrm{kPa}$	
	60	18.5	$1.3 \pm 0.1 \text{MPa}$	
	60	5.6	$148.3 \pm 25.0 \mathrm{kPa}$	
	60	7.4	$225.8 \pm 53.8 \mathrm{kPa}$	
	60	11.1	$337.5 \pm 59.8 \mathrm{kPa}$	
	60	14.8	$864.7 \pm 98.0 \mathrm{kPa}$	
	60	18.5	$1.3 \pm 0.1 \text{MPa}$	

3D, three-dimensional; DLP, digital light processing.

intensity used during printing. As the light intensity for photopolymerization increases, the kinetic chain length of PGSA decreases, forcing the PGSA polymer chains into a more restricted conformation. A4,71,72 As the crosslinking density increases, the available space for the PGSA polymer chains to move decreases, a4,72 resulting in an increased stiffness of the 3D printed scaffold.

Digital modulation of mechanical properties through the adjustment of 2PP parameters: printing speed, laser current, and infill density

Similar to the DLP-based printer, the 2PP printer has several printing parameters that can be manipulated to modulate the printed sample stiffness, including: (1) printing speed, (2) laser pump current, and (3) infill density.

To investigate the effect of the 2PP printing speed on the scaffold's Young's modulus, PGSA scaffolds were printed at 100, 300, and 500 μ m/s with a default setting of 50% infill and a current of 2.50 A. The resulting Young's modulus is shown on Table 2 and Figure 4A. A significant effect of the 2PP printing speed on scaffold stiffness was observed (p<0.0001). Sidak's *post hoc* multiple comparison tests revealed significant differences among all the 2PP printing speeds (p<0.0119).

To investigate the effect of the 2PP laser pump current on the scaffold's stiffness, we printed the PGSA scaffolds at a current of 2.0, 2.25, 2.50, and 2.65 A (equivalent laser power of 40, 58.5, 80.5, and 95.4 mW/cm²) with a default printing infill of 50% and a printing speed of 300 μ m/s. The resulting stiffnesses were shown on Table 2 and Figure 4B. A significant effect of 2PP printing current on scaffold's Young's modulus was observed (p < 0.0001), and *post hoc* tests demonstrated significant differences among all 2PP printing currents (p < 0.0025).

Table 2. Experimental Stiffness Measurements of Two-Photon Polymerization Printed Structure and the Corresponding Printing Parameters

		Printing parameters			
3D printing system	Print speed (µm/s)	Laser current (A)	Laser power (mW/cm ²)	Infill density (%)	Measured stiffness
2PP	100	2.5	80.5	50	$2.7 \pm 0.3 \text{MPa}$
	300	2.5	80.5	50	$942.8 \pm 38.7 \mathrm{kPa}$
	500	2.5	80.5	50	$618.2 \pm 50.9 \mathrm{kPa}$
	300	2.0	40	50	$396.7 \pm 42.9 \text{kPa}$
	300	2.25	58.5	50	$762.4 \pm 30.0 \mathrm{kPa}$
	300	2.5	80.5	50	$942.8 \pm 38.7 \mathrm{kPa}$
	300	2.65	95.4	50	$1.3 \pm 0.1 \text{MPa}$
	300	2.5	80.5	10	$67.1 \pm 17.5 \text{ kPa}$
	300	2.5	80.5	30	$396.5 \pm 102.3 \text{ kPa}$
	300	2.5	80.5	50	$942.8 \pm 38.7 \mathrm{kPa}$
	300	2.5	80.5	70	$1.6 \pm 0.2 \text{MPa}$

2PP, two-photon polymerization.

To investigate the effect of varying 2PP printing infill on printed structure's stiffness, we printed the PGSA scaffolds with an infill of 10%, 30%, 50%, and 70% with a printing speed and current kept constant at 300 μ m/s and 2.50 A, respectively. The resulting Young's moduli are shown on Table 2 and Figure 4C. A significant effect of 2PP printing infill on the scaffold's Young's modulus was observed (p < 0.0001). Sidak's *post hoc* tests also revealed significant differences among all 2PP printing infills (p < 0.0005). The effect of infill density on the stiffness can also be visually observed with variations in the resulting microstructure density through scanning electron microscope (SEM) (Supplementary Fig. S2).

Combining DLP-based 3D printing with 2PP 3D printing

An investigation to explore the potential to fabricate a more complex tissue engineering scaffold by combining DLP-based 3D printing with 2PP 3D printing was carried out following the method described in Combining DLP-based 3D printing with 2PP 3D printing. In this experiment, 2PP printed PGSA scaffolds printed at either 300 or 500 µm/s printing speed (50% infill, 2.50 A current) were fabricated on top of a soft DLP printed PGSA matrix, stiff DLP printed PGSA matrix, or a coverslip.

The soft DLP printed PGSA matrices were printed with a $30\,s$ exposure time and a light intensity of $18.5\,\text{mW/cm}^2$ with a Young's modulus of $67.1\pm5.9\,\text{kPa}$ (Fig. 4D and Table 1). The stiff DLP printed PGSA matrices were printed with $60\,s$ exposure time and light intensity of $18.5\,\text{mW/cm}^2$ with the Young's modulus of $1.3\pm0.1\,\text{MPa}$ (Fig. 4E and Table 1). The stiffness of the 2PP printed structure printed on top of the soft matrix, stiff matrix, and the coverslip at $300\,\mu\text{m/s}$ printing speed was $981.7\pm31.1\,\text{kPa}$, $948.4\pm22.3\,\text{kPa}$, and $942.8\pm38.7\,\text{kPa}$, respectively (Supplementary Fig. S3). The stiffness of the 2PP printed structure printed with $500\,\mu\text{m/s}$ on top of the soft matrix, stiff matrix, and the coverslip at $500\,\mu\text{m/s}$ printing speed was $623.6\pm43.8\,\text{kPa}$, $626.8\pm47.9\,\text{kPa}$, and $618.2\pm50.9\,\text{kPa}$, respectively (Supplementary Fig. S3).

These results suggest that 2PP printed structures could maintain their own individual local stiffness value according

to the specified printing parameter, independent of the base matrix's stiffness. Thus, the modular control of 2PP printed microstructure stiffness is possible in a multiprinter hybrid printing platform as the 2PP printed microstructure stiffness is independent of the DLP printed substrate stiffness.

Utilization of machine learning and NNs toward precise stiffness control of 3D printed scaffolds

The previous experiments verified that stiffness-modulated 3D scaffolds could be fabricated given a proper selection of printing parameters. With the application of machine learning, we want to extend the flexibility of mechanical property modulation on the domain of nonstandard printing parameter combinations. After training the NN as described in the Machine Learning section, the NN model generated a mapping from a variety of printing parameters to the expected sample stiffness for both the DLP printer and the 2PP printer (Fig. 5A, B). Once the parameter stiffness mapping was ready, a brute-force search could be applied to search for a user-defined stiffness and retrieve the printing parameters that could fabricate scaffold with such stiffness.

We further experimentally verify that the NN informed printing parameters could indeed yield the targeted stiffness. The printing parameters that correspond to the stiffness of 500 kPa and 1.0 MPa were generated from the machine learning module on the DLP-based 3D printer. The same approach was applied to the 2PP printer to print structures with targeted stiffness values of 125 kPa, 1.5 MPa, and 3 MPa. Then, the accuracy of the developed NN model was analyzed by comparing the targeted stiffness values with the actual stiffness of the scaffolds printed with those modelgenerated printing parameters. Note the selected validation stiffnesses were all unseen from the training data and were at least 100 kPa away from all the stiffnesses in the training dataset. The resulting model-generated parameters as well as the measured stiffness of the printed scaffolds are listed in Table 3 and compared in Figure 5.

The variances in the model predictions were also studied. The R^2 between the NN predicted and measured stiffness was 0.95, meaning that the majority of the variances on the measured mechanical properties were accounted for by the machine learning model (Fig. 5E).

Table 3.	THE NN MODEL-GENERATED PRINTING PARAMETERS AND CORRESPONDING
	TARGET STIFFNESS AND MEASURED STIFFNESS VALUES

3D printing system	NN-generated parameters	Target stiffness (MPa)	Measured stiffness (MPa)
DLP-based	Light intensity: 12.95 mW/cm ²	0.5	0.53 ± 0.025
	Exposure time: 59 s		
	Light intensity: 16.84 mW/cm ²	1.0	1.1 ± 0.062
	Exposure time: 59 s		
2PP	Infill: 36%	0.125	0.13 ± 0.014
	Printing current: 2.0 A (40 mW/cm ²)		
	Printing speed: 0.36 mm/s		
	Infill: 60%	1.5	1.5 ± 0.084
	Printing current: 2.29 A (61.8 mW/cm ²)		
	Printing speed: 0.22 mm/s		
	Infill: 63%	3.0	2.8 ± 0.26
	Printing current: 2.64 A (94.3 mW/cm ²)		
	Printing speed: 0.14 mm/s		

Multimodal light-based 3D printing with stiffness modulation

Once the machine learning model was trained on both the DLP and 2PP printers with PGSA sample stiffness measurements, an extended application could be applied to combine both printers for the fabrication of arbitrary DLP printed stiffness-modulated 3D macrostructures with stiffness-modulated microstructural features from 2PP printing. In this process, both the micro- and macrostructures can be modified with user-defined stiffness value by simply modifying the printing parameters of DLP and 2PP printers (Supplementary Fig. S4). The capability to modify the stiffness of both the microstructural features and the bulk macrostructure could enable future applications of precise fabrication of engineered tissue scaffolds with a range of adjustable mechanical properties.

As an example, the DLP printer was used to fabricate a ribbon scaffold, which was 125 μ m thick, \sim 100 μ m wide at the center and up to 1.2 mm wide at the two edges (Fig. 6). Then, engineered MTJ features, based on the TEM image of a native rat muscle-tendon tissue section, were fabricated on top of the center region of the ribbon scaffold. Microchannels measuring 6 µm in width were fabricated through 2PP 3D printing on the muscle side as an engineering design to aid muscle cell alignment, since promoting cellular alignment is an important factor in skeletal muscle tissue engineering. 73 This simple model could potentially help investigate the effect of different stiffness regions on muscle cell growth and migration. Furthermore, native stiffness of healthy and diseased tissues can be experimentally measured and incorporated into scaffolds to create better physiologically informed models of pathologic tissues.

Mouse myoblast (C2C12) viability

To ensure that this developed platform could be applied for tissue engineering applications, *in vitro* cell viability testing of C2C12 cells seeded on the PGSA scaffolds printed at different stiffness conditions was performed. C2C12 cells seeded on PGSA scaffolds with varying stiffnesses showed excellent cell viability (>95%) at days 1 and 7 after cell seeding (Supplementary Fig. S5).

Discussion

User-defined material properties in a scaffold are typically achieved through manual optimization of printing parameters, which consumes a large amount of time and resources. NN informed printing parameters to create scaffolds with user-defined material properties will allow for efficient fabrication of precision-engineered scaffolds. Our method demonstrated the ability to precisely control the stiffness of PGSA scaffolds in both the DLP-based and 2PP 3D printing systems through the variation of the light intensity, exposure time, printing infill, printing current, and printing speed. This would be highly beneficial in interfacial tissue engineering applications, such as muscle—tendon or tendon—bone scaffold engineering, ^{47–51} where stiffness gradients are present.

Previous studies have demonstrated the ability to tailor mechanical properties of crosslinked polymers through adjusting degree of acrylation, subjecting polymerized material to postprocessing methods, or creating a composite polymeric network. 44,46,49,50 While effective, these methods—such as synthesizing multiple formulations of PGSA with different degrees of acrylation—are time-consuming and economically inefficient. In addition, the precision tuning of scaffold material properties and precise deposition of these materials can be challenging. By simply adjusting the printing parameters, our method shows the potential to quickly fabricate a 3D printed scaffold with heterogeneous local mechanical properties from a single bioink. This may lead to the fabrication of tissue engineering scaffolds aiming to mimic the complex milieu of interfacial tissues.

To minimize the error between targeted stiffnesses and measured stiffnesses, one could potentially apply the training data collection on a larger set of printing parameters. In addition, this machine learning workflow is easily translatable to other materials as well as printing systems.

By combining the two printing platforms, the rapid fabrication speed of the DLP-based 3D printer for a bulk structure and the submicron resolution of the 2PP 3D printer for fine detailing can be simultaneously exploited. This allows one to fabricate more complex scaffolds with "larger" geometrical and mechanical cues fabricated with DLP-based printer complemented with "smaller" submicron geometrical and mechanical cues fabricated with 2PP printing, taking advantage of the strengths of both printing platforms.

In conclusion, this study investigated mechanisms of scaffold stiffness modulation using multimodal light-based 3D printing and a NN-based machine learning approach. Control of material properties using both DLP-based and 2PP 3D printing systems with a range of stiffness over two orders of magnitude was achieved within the same biomaterial. In addition, a hybrid printing system utilizing both the DLP-based and 2PP 3D printing systems was used to fabricate scaffolds with multiscale resolution and spatial stiffness heterogeneity. Furthermore, the ability to precision tune 3D printed scaffold with user-defined material properties using a machine learning algorithm trained on experimental data was showcased. The flexibility of adjusting the printing parameters allows not only user-defined adjustment of stiffness, but also local regional stiffness of the printed scaffold, which enables us to fabricate complex microstructures with customizable stiffness distributions. This approach lays the foundation for future studies in areas where fine control over both geometry and mechanical properties is required, such as interfacial tissue engineering applications.

Data Availability

All data are available upon reasonable request to the corresponding author.

Disclosure Statement

No competing financial interests exist.

Funding Information

This work was supported in part by grants from the National Science Foundation (NSF; 1907434, 2135720, 2026236). This work was performed in part at the San Diego Nanotechnology Infrastructure (SDNI) of University of California San Diego (UCSD), a member of the National Nanotechnology Coordinated Infrastructure, which is supported by the NSF (Grant ECCS-2025752). W.K. is supported by the Anandamahidol Foundation. We also acknowledge the support from Cellink for its bioprinter (BIONONA X). The authors thank the University of California, San Diego—Cellular and Molecular Medicine Electron Microscopy Core (UCSD-CMM-EM Core, RRID: SCR_022039) for equipment access and technical assistance. The UCSD-CMM-EM Core is partly supported by the National Institutes of Health Award number S10OD023527.

Supplementary Material

Supplementary Figure S1 Supplementary Figure S2

Supplementary Figure S3

Supplementary Figure S4

Supplementary Figure S5

References

- Ma X, Liu J, Zhu W, et al. 3D bioprinting of functional tissue models for personalized drug screening and in vitro disease modeling. Adv Drug Deliv Rev 2018;132:235–251; doi: 10.1016/j.addr.2018.06.011
- 2. Zhong Z, Wang J, Tian J, et al. Rapid 3D bioprinting of a multicellular model recapitulating pterygium microenvi-

- ronment. Biomaterials 2022;282:121391; doi: 10.1016/j .biomaterials.2022.121391
- 3. Miller KL, Xiang Y, Yu C, et al. Rapid 3D BioPrinting of a human iPSC-derived cardiac micro-tissue for high-throughput drug testing. Organs Chip 2021;3:100007; doi: 10.1016/j.ooc.2021.100007
- Tang M, Tiwari SK, Agrawal K, et al. Rapid 3D bioprinting of glioblastoma model mimicking native biophysical heterogeneity. Small 2021;17(15):e2006050; doi: 10.1002/ smll.202006050
- Zhong Z, Deng X, Wang P, et al. Rapid bioprinting of conjunctival stem cell micro-constructs for subconjunctival ocular injection. Biomaterials 2021;267:120462; doi: 10 .1016/j.biomaterials.2020.120462
- Wangpraseurt D, You S, Azam F, et al. Bionic 3D printed corals. Nat Commun 2020;11(1):1748; doi: 10.1038/ s41467-020-15486-4
- 7. Koffler J, Zhu W, Qu X, et al. Biomimetic 3D-printed scaffolds for spinal cord injury repair. Nat Med 2019;25: 263–269; doi: 10.1038/s41591-018-0296-z
- 8. Yu C, Ma X, Zhu W, et al. Scanningless and continuous 3D bioprinting of human tissues with decellularized extracellular matrix. Biomaterials 2019;194:1–13; doi: 10.1016/j.biomaterials.2018.12.009
- Zhu W, Tringale KR, Woller SA, et al. Rapid continuous 3D printing of customizable peripheral nerve guidance conduits. Mater Today 2018;21(9):951–959; doi: 10.1016/j .mattod.2018.04.001
- Xue D, Wang Y, Zhang J, et al. Projection-based 3D printing of cell patterning scaffolds with multiscale channels. ACS Appl Mater Interfaces 2018;10(23):19428–19435; doi: 10.1021/acsami.8b03867
- Ma X, Yu C, Wang P, et al. Rapid 3D bioprinting of decellularized extracellular matrix with regionally varied mechanical properties and biomimetic microarchitecture. Biomaterials 2018;185:310–321; doi: 10.1016/j .biomaterials.2018.09.026
- 12. Zhu W, Qu X, Zhu J, et al. Direct 3D bioprinting of prevascularized tissue constructs with complex microarchitecture. Biomaterials 2017;124:106–115; doi: 10 .1016/j.biomaterials.2017.01.042
- 13. Kiratitanaporn W, Berry DB, Mudla A, et al. 3D printing a biocompatible elastomer for modeling muscle regeneration after volumetric muscle loss. Biomater Adv 2022;142: 213171; doi: 10.1016/j.bioadv.2022.213171
- 14. Tang M, Xie Q, Gimple RC, et al. Three-dimensional bioprinted glioblastoma microenvironments model cellular dependencies and immune interactions. Cell Res 2020;30(10):833–853; doi: 10.1038/s41422-020-0338-1
- 15. Hermida MA, Kumar JD, Schwarz D, et al. Three dimensional in vitro models of cancer: Bioprinting multilineage glioblastoma models. Adv Biol Regul 2020;75:100658; doi: 10.1016/j.jbior.2019.100658
- Zhao H, Xu J, Yuan H, et al. 3D printing of artificial skin patches with bioactive and optically active polymer materials for anti-infection and augmenting wound repair. Mater Horizons 2022;9(1):342–349; doi: 10.1039/d1mh00508a
- 17. Jia W, Gungor-Ozkerim PS, Zhang YS, et al. Direct 3D bioprinting of perfusable vascular constructs using a blend bioink. Biomaterials 2016;106:58–68; doi: 10.1016/j.biomaterials.2016.07.038
- Cubo N, Garcia M, Del Cañizo JF, et al. 3D bioprinting of functional human skin: Production and in vivo analysis. Biofabrication 2017;9(1):015006; doi: 10.1088/1758-5090/ 9/1/015006

 Ren J, Han P, Ma X, et al. Canonical Wnt5b signaling directs outlying Nkx2.5⁺ mesoderm into pacemaker cardiomyocytes. Dev Cell 2019;50(6):729.e5–743.e5; doi: 10 .1016/J.DEVCEL.2019.07.014

- Ma X, Qu X, Zhu W, et al. Deterministically patterned biomimetic human iPSC-derived hepatic model via rapid 3D bioprinting. Proc Natl Acad Sci U S A 2016;113(8)2206– 2211; doi: 10.1073/pnas.1524510113
- 21. Liu J, Miller K, Ma X, et al. Direct 3D bioprinting of cardiac micro-tissues mimicking native myocardium. Biomaterials 2020;256:120204; doi: 10.1016/j.biomaterials .2020.120204
- 22. Peper S, Vo T, Ahuja N, et al. Bioprinted nanocomposite hydrogels: A proposed approach to functional restoration of skeletal muscle and vascular tissue following volumetric muscle loss. Curr Opin Pharmacol 2021;58:35–43; doi: 10.1016/j.coph.2021.03.005
- 23. Lee H, Kim W, Lee J, et al. Self-aligned myofibers in 3D bioprinted extracellular matrix-based construct accelerate skeletal muscle function restoration. Appl Phys Rev 2021;8(2):021405; doi: 10.1063/5.0039639
- Kim Y, Yang Y, Zhang X, et al. Remote control of muscledriven miniature robots with battery-free wireless optoelectronics. Sci Robot 2023;8(74):eadd1053; doi: 10.1126/ scirobotics.add1053
- 25. Fornetti E, De Paolis F, Fuoco C, et al. A novel extrusion-based 3D bioprinting system for skeletal muscle tissue engineering. Biofabrication 2023;15(2):25009; doi: 10.1088/1758-5090/acb573
- Byambaa B, Annabi N, Yue K, et al. Bioprinted osteogenic and vasculogenic patterns for engineering 3D bone tissue. Adv Healthc Mater 2017;6(16):1–15; doi: 10.1002/adhm .201700015
- Inzana JA, Olvera D, Fuller SM, et al. 3D printing of composite calcium phosphate and collagen scaffolds for bone regeneration. Biomaterials 2014;35(13):4026–4034; doi: 10.1016/j.biomaterials.2014.01.064
- 28. Farris AL, Lambrechts D, Zhou Y, et al. 3D-printed oxygen-releasing scaffolds improve bone regeneration in mice. Biomaterials 2022;280:121318; doi: 10.1016/j.biomaterials.2021.121318
- Sarkar N, Zhou Y, Grayson W. 3D Printing for Craniofacial Bone Regeneration. In: 3D Bioprinting and Nanotechnology in Tissue Engineering and Regenerative Medicine (Second Edition). (Zhang LG, Fisher JP, Leong KW. eds.) Academic Press: Cambridge, MA; 2022; pp. 311–335; doi: 10.1016/B978-0-12-824552-1.00008-6
- 30. Xu F, Celli J, Rizvi I, et al. A three-dimensional in vitro ovarian cancer coculture model using a high-throughput cell patterning platform. Biotechnol J 2011;6(2):204–212; doi: 10.1002/biot.201000340
- 31. Tang M, Rich JN, Chen S. Biomaterials and 3D bioprinting strategies to model glioblastoma and the blood–brain barrier. Adv Mater 2021;33(5):1–25; doi: 10.1002/adma.202004776
- 32. Meng F, Meyer CM, Joung D, et al. 3D bioprinted in vitro metastatic models via reconstruction of tumor microenvironments. Adv Mater 2019;31(10):e1806899; doi: 10.1002/adma.201806899
- 33. Singh D, Harding AJ, Albadawi E, et al. Additive manufactured biodegradable poly(glycerol sebacate methacrylate) nerve guidance conduits. Acta Biomater 2018;78:48–63; doi: 10.1016/j.actbio.2018.07.055
- 34. Wang P, Berry D, Moran A, et al. Controlled growth factor release in 3D-printed hydrogels. Adv Healthc Mater 2020;9(15):1–9; doi: 10.1002/adhm.201900977

 Frantz C, Stewart KM, Weaver VM. The extracellular matrix at a glance. J Cell Sci 2010;123(24):4195–4200; doi: 10.1242/jcs.023820

- 36. Garg K, Ward CL, Rathbone CR, et al. Transplantation of devitalized muscle scaffolds is insufficient for appreciable de novo muscle fiber regeneration after volumetric muscle loss injury. Cell Tissue Res 2014;358(3):857–873; doi: 10 .1007/s00441-014-2006-6
- 37. Rørth P. Whence directionality: Guidance mechanisms in solitary and collective cell migration. Dev Cell 2011;20(1): 9–18; doi: 10.1016/j.devcel.2010.12.014
- 38. Altomare L, Gadegaard N, Visai L, et al. Biodegradable microgrooved polymeric surfaces obtained by photolithography for skeletal muscle cell orientation and myotube development. Acta Biomater 2010;6(6):1948–1957; doi: 10.1016/j.actbio.2009.12.040
- Chen CS, Mrksich M, Huang S, et al. Geometric control of cell life and death. Science (80-) 1997;276(5317):1425– 1428; doi: 10.1126/science.276.5317.1425
- Li D, Zhou J, Chowdhury F, et al. Role of mechanical factors in fate decisions of stem cells. Regen Med 2011;6(2):229–240; doi: 10.2217/rme.11.2
- 41. Ghasemi-Mobarakeh L. Structural properties of scaffolds: Crucial parameters towards stem cells differentiation. World J Stem Cells 2015;7(4):728; doi: 10.4252/wjsc.v7.i4 .728
- 42. Engler AJ, Sen S, Sweeney HL, et al. Matrix elasticity directs stem cell lineage specification. Cell 2006;126(4): 677–689; doi: 10.1016/j.cell.2006.06.044
- Nikkhah M, Edalat F, Manoucheri S, et al. Engineering microscale topographies to control the cell-substrate interface. Biomaterials 2012;33(21):5230–5246; doi: 10.1016/j .biomaterials.2012.03.079
- 44. Wang P, Berry DB, Song Z, et al. 3D printing of a biocompatible double network elastomer with digital control of mechanical properties. Adv Funct Mater 2020;30(14):1–9; doi: 10.1002/adfm.201910391
- Nijst CLE, Bruggeman JP, Karp JM, et al. Synthesis and characterization of photocurable elastomers from poly(glycerol-co-sebacate). Biomacromolecules 2007;8(10): 3067–3073; doi: 10.1021/bm070423u
- 46. Wu YL, D'Amato AR, Yan AM, et al. Three-dimensional printing of poly(glycerol sebacate) acrylate scaffolds via digital light processing. ACS Appl Bio Mater 2020;3(11): 7575–7588; doi: 10.1021/acsabm.0c00804
- 47. Merceron TK, Burt M, Seol YJ, et al. A 3D bioprinted complex structure for engineering the muscle-tendon unit. Biofabrication 2015;7(3):035003; doi: 10.1088/1758-5090/7/3/035003
- 48. Freedman BR, Kuttler A, Beckmann N, et al. Enhanced tendon healing by a tough hydrogel with an adhesive side and high drug-loading capacity. Nat Biomed Eng 2022;6(10):1167–1179; doi: 10.1038/s41551-021-00810-0
- Yao Z, Qian Y, Jin Y, et al. Biomimetic multilayer polycaprolactone/sodium alginate hydrogel scaffolds loaded with melatonin facilitate tendon regeneration. Carbohydr Polym 2022;277:118865; doi: 10.1016/j.carbpol.2021 .118865
- No YJ, Tarafder S, Reischl B, et al. High-strength fiberreinforced composite hydrogel scaffolds as biosynthetic tendon graft material. ACS Biomater Sci Eng 2020;6(4): 1887–1898; doi: 10.1021/acsbiomaterials.9b01716
- 51. Jiang X, Wu S, Kuss M, et al. 3D printing of multilayered scaffolds for rotator cuff tendon regeneration. Bioact Mater 2020;5(3):636–643; doi: 10.1016/j.bioactmat.2020.04.017

- 52. Pashneh-Tala S, Owen R, Bahmaee H, et al. Synthesis, characterization and 3D micro-structuring via 2-photon polymerization of poly(glycerol sebacate)-methacrylate—An elastomeric degradable polymer. Front Phys 2018;6:41; doi: 10.3389/fphy.2018.00041
- 53. Rai R, Tallawi M, Barbani N, et al. Biomimetic poly(glycerol sebacate) (PGS) membranes for cardiac patch application. Mater Sci Eng C 2013;33(7):3677–3687; doi: 10.1016/j.msec.2013.04.058
- 54. Motlagh D, Yang J, Lui KY, et al. Hemocompatibility evaluation of poly(glycerol-sebacate) in vitro for vascular tissue engineering. Biomaterials 2006;27(24):4315–4324; doi: 10.1016/j.biomaterials.2006.04.010
- 55. Guillemette MD, Park H, Hsiao JC, et al. Combined technologies for microfabricating elastomeric cardiac tissue engineering scaffolds. Macromol Biosci 2010;10(11): 1330–1337; doi: 10.1002/mabi.201000165
- Yeh Y-C, Highley CB, Ouyang L, et al. 3D printing of photocurable poly(glycerol sebacate) elastomers. Biofabrication 2016;8(4):045004; doi: 10.1088/1758-5090/8/4/ 045004
- Wang Y, Ameer GA, Sheppard BJ, et al. A tough biodegradable elastomer. Nat Biotechnol 2002;20(6):602–606; doi: 10.1038/nbt0602-602
- Chen Q-Z, Ishii H, Thouas GA, et al. An elastomeric patch derived from poly(glycerol sebacate) for delivery of embryonic stem cells to the heart. Biomaterials 2010;31(14): 3885–3893; doi: 10.1016/J.BIOMATERIALS.2010.01.108
- 59. Tamayol A, Hassani Najafabadi A, Mostafalu P, et al. Biodegradable elastic nanofibrous platforms with integrated flexible heaters for on-demand drug delivery. Sci Rep 2017;7(1):1–10; doi: 10.1038/s41598-017-04749-8
- 60. Chen Q-Z, Bismarck A, Hansen U, et al. Characterisation of a soft elastomer poly(glycerol sebacate) designed to match the mechanical properties of myocardial tissue. Biomaterials 2008;29(1):47–57; doi: 10.1016/J.BIOMATERIALS.2007.09.010
- 61. Pereira MJN, Ouyang B, Sundback CA, et al. A highly tunable biocompatible and multifunctional biodegradable elastomer. Adv Mater 2013;25(8):1209–1215; doi: 10.1002/adma.201203824
- 62. Goh GD, Sing SL, Yeong WY. A review on machine learning in 3D printing: Applications, potential, and challenges. Artif Intell Rev 2021;54(3):1–32; doi: 10.1007/s10462-020-09876-9
- 63. You S, Guan J, Alido J, et al. Mitigating scattering effects in light-based three-dimensional printing using machine learning. J Manuf Sci Eng 2020;142(8):081002; doi: 10.1115/1.4046986
- 64. Guan J, You S, Xiang Y, et al. Compensating the cellinduced light scattering effect in light-based bioprinting

- using deep learning. Biofabrication 2022;14(1):015011; doi: 10.1088/1758-5090/ac3b92
- 65. Kontomaris SV, Malamou A. Hertz model or Oliver & Pharr analysis? Tutorial regarding AFM nanoindentation experiments on biological samples. Mater Res Express 2020;7(3):033001; doi: 10.1088/2053-1591/ab79ce
- 66. Marsano A, Maidhof R, Wan LQ, et al. Scaffold stiffness affects the contractile function of three-dimensional engineered cardiac constructs. Biotechnol Prog 2010;26(5): 1382–1390; doi: 10.1002/btpr.435
- Goodfellow I, Bengio Y, Courville A. Deep Learning. MIT Press: Cambridge, MA; 2016.
- 68. Fukushima K. Cognitron: A self-organizing multilayered neural network. Biol Cybern 1975;20(3–4):121–136; doi: 10.1007/BF00342633
- 69. Paszke A, Gross S, Massa F, et al. PyTorch: An imperative style high performance deep learning library. NeurIPS. In: Advances in Neural Information Processing Systems. Curran Associates, Inc.: Vancouver, Canada; 2019; 32. Available from: https://proceedings.neurips.cc/paper_files/paper/2019/file/bdbca288fee7f92f2bfa9f7012727740-Paper.pdf [Last accessed: October 12, 2023].
- Kingma DP, Ba J. Adam: A method for stochastic optimization. arXiv preprint arXiv:1412.6980. 2014; doi: 10.48550/arXiv.1412.6980
- 71. Pyo SH, Wang P, Hwang HH, et al. Continuous optical 3D printing of green aliphatic polyurethanes. ACS Appl Mater Interfaces 2017;9(1):836–844; doi: 10.1021/acsami .6b12500
- 72. Decker C. Kinetic study and new applications of UV radiation curing. Macromol Rapid Commun 2002;23(18): 1067–1093; doi: 10.1002/marc.200290014
- 73. Sicari BM, Dearth CL, Badylak SF. Tissue engineering and regenerative medicine approaches to enhance the functional response to skeletal muscle injury. Anat Rec 2014;297(1): 51–64; doi: 10.1002/ar.22794

Address correspondence to:
Shaochen Chen, PhD
Department of Nanoengineering
University of California San Diego
9500 Gilman Drive
La Jolla, CA 92093
USA

E-mail: shc064@ucsd.edu

Received: July 31, 2023 Accepted: September 20, 2023 Online Publication Date: October 24, 2023